Int. J. Radiation Oncology Biol. Phys., Vol. 51, No. 1, pp. 227–243, 2001
Copyright © 2001 Elsevier Science Inc.
Printed in the USA. All rights reserved
0360-3016/01/$–see front matter

PII S0360-3016(01)01667-4

PHYSICS CONTRIBUTION

IMAGE-BASED DOSE PLANNING OF INTRACAVITARY BRACHYTHERAPY: REGISTRATION OF SERIAL-IMAGING STUDIES USING DEFORMABLE ANATOMIC TEMPLATES

GARY E. CHRISTENSEN, D.SC.,* BLAKE CARLSON, M.S.,* K. S. CLIFFORD CHAO, M.D.,† PEN YIN, M.S.,* PERRY W. GRIGSBY, M.D.,† KIM NGUYEN,† JAMES F. DEMPSEY, PH.D.,† FRITZ A. LERMA, PH.D.,† KYONGTAE T. BAE, M.D.,† MICHAEL W. VANNIER, M.D.,‡ AND JEFFREY F. WILLIAMSON, PH.D.†

Departments of *Electrical Engineering and ‡Radiology, University of Iowa, Iowa City, IA; †Radiation Oncology Center, Washington University, St. Louis, MO

Purpose: To demonstrate that high-dimensional voxel-to-voxel transformations, derived from continuum mechanics models of the underlying pelvic tissues, can be used to register computed tomography (CT) serial examinations into a single anatomic frame of reference for cumulative dose calculations.

Methods and Materials: Three patients with locally advanced cervix cancer were treated with CT-compatible intracavitary (ICT) applicators. Each patient underwent five volumetric CT examinations: before initiating treatment, and immediately before and after the first and second ICT insertions, respectively. Each serial examination was rigidly registered to the patient's first ICT examination by aligning the bony anatomy. Detailed nonrigid alignment for organs (or targets) of interest was subsequently achieved by deforming the CT exams as a viscous-fluid, described by the Navier-Stokes equation, until the coincidence with the corresponding targets on CT image was maximized. In cases where ICT insertion induced very large and topologically complex rearrangements of pelvic organs, e.g., extreme uterine canal reorientation following tandem insertion, a viscous-fluid-landmark transformation was used to produce an initial registration.

Results: For all three patients, reasonable registrations for organs (or targets) of interest were achieved. Fluid-landmark initialization was required in 4 of the 11 registrations. Relative to the best rigid bony landmark alignment, the viscous-fluid registration resulted in average soft-tissue displacements from 2.8 to 28.1 mm, and improved organ coincidence from the range of 5.2% to 72.2% to the range of 90.6% to 100%. Compared to the viscous-fluid transformation, global registration of bony anatomy mismatched 5% or more of the contoured organ volumes by 15–25 mm.

Conclusion: Pelvic soft-tissue structures undergo large deformations and displacements during the external-beam and multiple-ICT course of radiation therapy for locally advanced cervix cancer. These changes cannot be modeled by the conventional rigid landmark transformation method. In the current study, we found that the deformable anatomic template registration method, based on continuum-mechanics models of deformation, successfully described these large anatomic shape changes before and after ICT. These promising modeling results indicate that realistic registration of the cumulative dose distribution to the organs (or targets) of interest for radiation therapy of cervical cancers is achievable. © 2001 Elsevier Science Inc.

Internal organ motion, Image registration, Cervix cancer, Continuum mechanical registration, Brachytherapy.

INTRODUCTION

Radiation therapy is an effective treatment modality for carcinoma of the cervix, with 5-year survivals ranging from approximately 60% for FIGO Stage IIB to 10% for Stage IVB (1). In most clinical systems, most of the central dose is delivered by means of intracavitary brachytherapy (ICT) (2, 3). Although many massive tumors are cured by radiation therapy alone, local recurrence rates for Stage IB to IIIB radiotherapy-alone patients ranges from 2% to 40% (4–6). While metastatic disease is a significant cause of mortality for these patients, achieving local control for locally advanced lesions remains a problem. Even with the addition of concomitant chemotherapy, the locoregional failure rate in the presence of bulky tumors remains significant (7), indicating the imminent need for further improvement. In addition, definitive radiation therapy, with or without concurrent chemotherapy, results in significant grade

Reprint requests to: Prof. Jeffrey F. Williamson, Ph.D., Washington University School of Medicine, Radiation Oncology Center, Mallinckrodt Institute of Radiology, 510 S. Kingshighway Boulevard, St. Louis, MO 63110. Tel: (314) 362-2267; Fax: (314) 362-2682; E-mail: Williamson_jf@castor.wustl.edu

This work was presented at the 42nd Annual ASTRO Meeting, Boston, MA, October 22–26, 2000.

This work was supported by NIH grant R01–CA75371.

Received Jan 9, 2001, and in revised form May 7, 2001. Accepted for publication May 15, 2001.

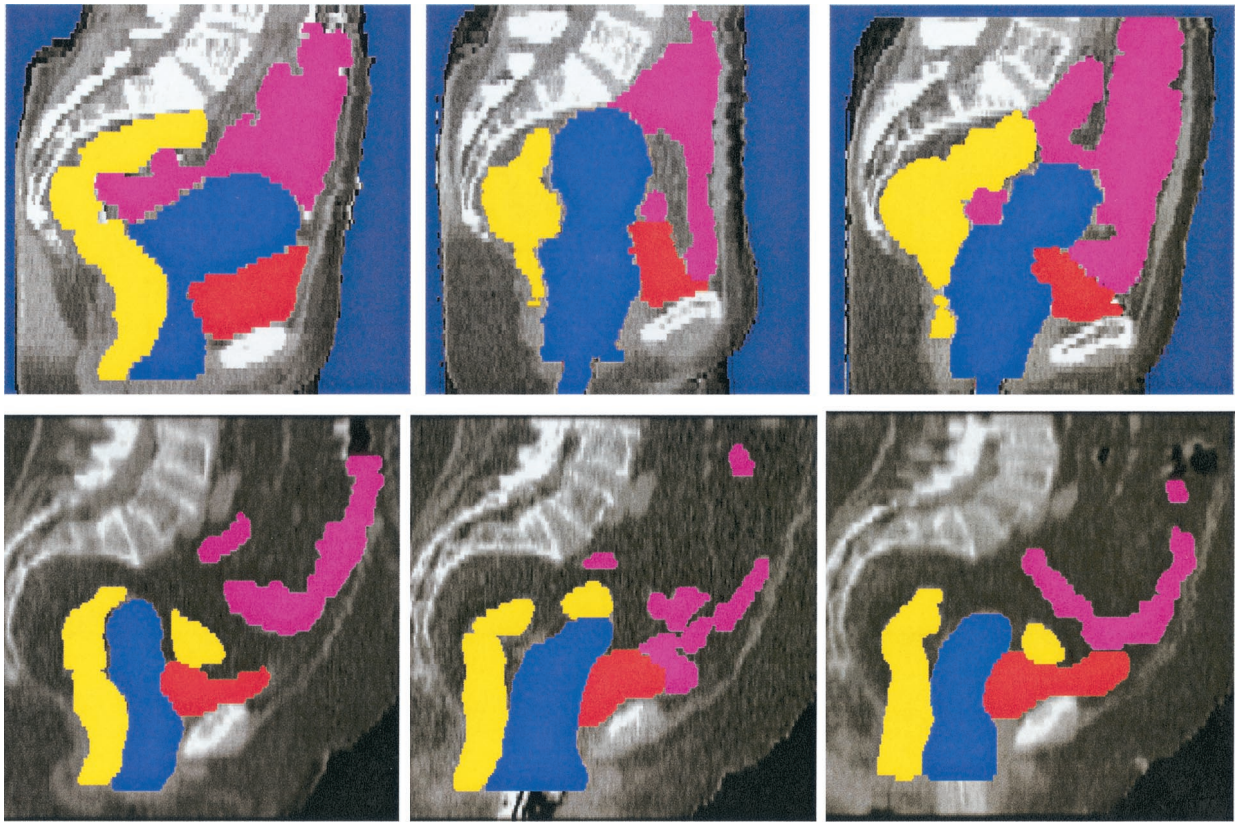

Fig. 1. Midline sagittal reconstruction of studies A, C, and E (columns 1–3, respectively) for patient 1 (lower row) and patient 3 (upper row). The images illustrate the binary masks used represent the contoured anatomical structures.

III/IV normal-tissue complication rates (10%-30% [7–10]). The combination of potential radiocurability of locally advanced lesions, high local failure rates, and high rates of late normal-tissue complications suggests that physical optimization of radiation therapy to the pelvis may eventually improve the therapeutic outcome.

The potential for improving local control using currently available planning and dose specification methods is limited. Because computed tomography (CT) or magnetic resonance (MR) imaging has not been used to guide ICT applicator insertion and dose specification, localization of conventional reference points (Point A and bladder/rectal reference points [11]) neglects the complex three-dimensional (3D) spatial arrangement of pelvic organs. Several small studies comparing single-insertion dose calculations based on 3D anatomy derived from CT imaging, which are based upon conventional orthogonal film-based planning, show that conventional reference points, on average, overestimate minimum doses to the cervix by 67% (range 11–100%) (12) and underestimate maximum doses to critical structures by factors of 1.9–2.3 (12–15). It is not surprising that dose-response data based on orthogonal film-based dosimetry are often contradictory, with some studies indicating no dependence or a very weak dependence of complication or recurrence rates upon reference-point doses (8, 9).

Despite the evident potential for image-based ICT dose planning to improve the correlation between dose specification and clinical outcome, such applications of 3D imaging have been limited due to the difficulty of registering serial-imaging studies. For example, insertion of intracavitary applicators can dramatically alter the geometry of normal tissues and target tumor structures (See Fig. 1). In addition, because of tumor regression during the course of irradiation and variability in implant insertion and packing techniques, the bladder and rectum are likely to differ in shape and location relative to the applicators from insertion-to-insertion. However, to meaningfully predict a patient's response to a course of treatment, the cumulative physical or biologic dose at each tissue voxel in each organ system at risk must be specified. This requires voxel-to-voxel registration of serial CT or MR imaging studies with and without implant applicators. By quantifying applicator displacements from one insertion to the next, relative to bony anatomy visualized on orthogonal radiographs, we have found that linear shifts can be as large as 26 mm (16, 17). Such shifts were associated with differences in reference point doses ranging from 33% to 88% (16, 18). Given the 8–15%/mm dose gradients around intracavitary implants, image-based dose optimization and planning are destined to fail, without rigorously accounting for the variable displacements of normal tissue structures during radiotherapy treatment. We believe that inability to address the problem of normal tissue registration from one imaging study to the

next is the main reason that so little progress has been made in applying imaging-based treatment planning to radiation therapy for cervix cancer.

To solve the serial image registration problem associated with multiple-insertion courses of ICT and external-beam therapy, we have used a deformable image-mapping technique to map serial CT images, each representing one component of the treatment course, to each other (19). This approach uses continuum mechanics to model the nonrigid deformation of normal structures on one CT study relative to another, resulting in a high-dimensional voxel-to-voxel transformation to bring two imaging studies into registration. This technique, which we call the "viscous-fluid transformation algorithm," has been successfully implemented in neuroimaging (20). In contrast, previous work in image registration for radiation oncology treatment planning is largely limited to use of rigid-body or affine transformations to map each voxel of the first imaging study to its corresponding location in the second (21, 22). Whereas this approach accounts for global parameters (translation, rotation, scaling, etc.), it assumes that the matching anatomic structures are nondeformable and cannot be displaced from their relative positions from one another. We will show that this approach cannot account for the highly local and variable tissue displacements encountered in brachytherapy. The viscous-fluid transformation method (19) can accommodate the complex and highly localized spatial variability in interstudy voxel-to-voxel correspondence (19). Our approach (23) minimizes incorrect registration by using a coarse, low-dimensional registration to provide initial conditions for subsequent fine, high-dimensional registration. Precursors to our approach include Bookstein (24), who introduced landmark-based thin-plate spline image registration, and Bajcsy (25), who first modeled image-to-image registration as the deformation of a linear elastic solid.

METHODS AND MATERIALS

Patient material

A prospective nonrandomized clinical study of image-based treatment planning for definitive radiotherapy of locally advanced cervix carcinoma was initiated in 1999. Patients had histologically proven carcinoma of the uterine cervix (bulky Stage IB, IIB, or IIIB) and had been prescribed our standard radiotherapy regimen (26) for surgically-intact tumors (20 Gy to whole-pelvic fields, 30 Gy split-field, two low-dose-rate ICT, insertions each delivering 32.5 Gy to Point A, followed by 11 Gy from pelvic-sidewall boost fields). Patient subjects agreed to participate in five additional CT imaging studies as follows: study A, before initiating external beam therapy; studies B and C, immediately before and after the first intracavitary insertion; and studies D and E, immediately before and after the second insertion. CT imaging was performed on a spiral CT scanner PQ-2000 CT simulator (Marconi Medical Systems, Inc., Highland Heights, OH), using 3-mm-thick slices spaced at 3-mm intervals. The 512 × 512 images had an in-plane resolution of 0.9 × 0.9 mm. Three hundred mL of oral contrast was administered 30–45 min before scanning. To visualize the posterior vaginal wall and the bladder neck, a dilute solution of iodated contrast material was used for saturating the packing material and inflating the Foley catheter bulb. CT-compatible Fletcher-Suit applicators (27), consisting of aluminum tandems and colpostat bodies with afterloading tungsten shields, were used to obtain artifact-free images. The vagina, uterus, cervix, rectum, colon, bladder, and small bowel were manually contoured on each CT-slice image set by the project's participating dosimetrist (K.N.), using a virtual simultion workstation VoxelQ (Marconi Medical Systems, Inc.) associated with the CT scanner. These manual segmentations were then reviewed and corrected by a radiologist (T.B.) and radiation oncologist (K.S.C.).

In this study, we report on the first three patients accrued to our study. Patients 1 and 2 both had Stage IIIB disease and were treated with a tandem and Delclos mini-colpostats during the first insertion, and with a tandem and vaginal cylinder during the second insertion. Patient 3, who had Stage IIB disease, was treated with Fletcher colpostats and tandem during both insertions. Figure 1 illustrates the images (Studies A, C, and E) acquired for patients 1 and 3 before initiating therapy and immediately after the first and second ICT insertions.

Problem statement

Using five CT examinations (A-E) and associated manual segmentations, we aimed to track the soft-tissue deformation of the bladder, sigmoid/rectum, and uterus/vagina over the course of the treatment, for the purpose of computing the cumulative radiation dose administered to each of these structures. Each imaging study, including the manually-contoured structures, can be described as a multimodality image set:

$$\vec{I}_i(\vec{x}) = \begin{bmatrix} T_{i1}(\vec{x}) \\ T_{i2}(\vec{x}) \\ T_{i3}(\vec{x}) \\ T_{i4}(\vec{x}) \end{bmatrix} = \begin{bmatrix} \text{Gray scale CT image of study i} \\ \text{Bladder binary mask of study i} \\ \text{Vagina/uterus binary mask of study i} \\ \text{Rectum binary mask of study i} \end{bmatrix} \tag{1}$$

for $i \in \{A,B,C,D,E\}$ and $\vec{x} \in \Omega = [0,1]^3$. The subimages $T_{i2}(\vec{x}), T_{i3}(\vec{x})$, $T_{i4}(\vec{x})$ describe manually-contoured structures in terms of binary mask images, i.e., $T_{ik}(\vec{x}) = 1$ if x is in or on the contoured structure, and zero otherwise. The subimage $T_{i1}(x)$ describes the anatomy in terms of gray-scale intensity at each location $\vec{x}$ lying outside the binary masks. $T_{i1}(\vec{x})$ is equal to the CT Hounsfield number if $\vec{x}$ lies outside the binary masks, or zero if $\vec{x}$ lies within one of the binary masks. The CT intensities are masked by the segmentations in this manner to force the algorithm to match contoured boundaries rather than gray-scale anatomy within.

In the case of registering binary images, the gradient of

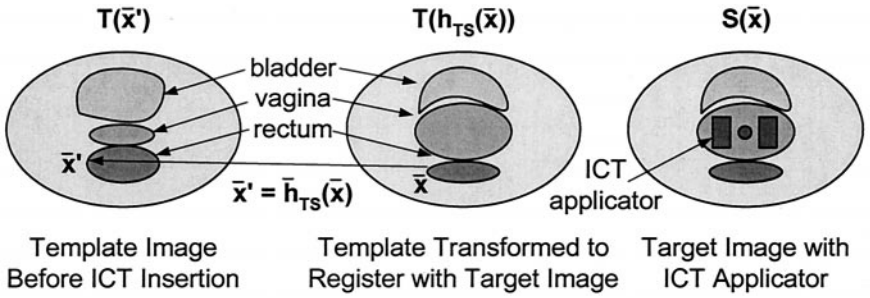

Fig. 2. Example of registering template image T to the target image S using the transformation $\vec{x} = \vec{h}_{TS}(\vec{t})$. Image $T(\vec{h}_{TS}(\vec{t}))$ is the transformation of image T by the transformation $\vec{h}_{TS}$ to look like image S.

the intensity cost function is nonzero only at the boundary of the objects; therefore, matching the intensities has the effect of matching the contours of the objects.

This makes it possible to match serial CT studies containing different objects such as:

1. ICT applicators present on some, but not all studies.
2. CT studies showing different types of applicators.
3. CT studies with variable rectal or bladder contents.
4. CT studies exhibiting varying degrees of contrast enhancement.

Associated with each study $\vec{T}_i(\vec{x})$ is an ICT insertion or series of external-beam fractions described by a 3D dose matrix, $D_i(\vec{x})$, $i \in \{A,B,C,D,E\}$, in one-to-one correspondence with the study. To compute the cumulative dose matrix, the dose matrices must be mapped into a common coordinate system. This is accomplished by estimating the vector-valued transformations $\vec{h}_{ij}:\Omega \rightarrow \Omega$, $i, j \in \{A,B,C,D,E\}$ that define the pointwise correspondence between the images in study i and those in study j as a function of the coordinate system of study j. Given these transformations, the cumulative dose distribution is computed in the coordinate system of study C by the formula

$$D_{\text{Total}}(\vec{x}) = D_C(\vec{x}) + \sum_{i\in\{\text{A,B,D,E}\}} D_i(\vec{h}_{iC}(\vec{x})). \qquad (2)$$

The process of deforming an image T into one-to-one correspondence with a target image S is illustrated in Fig. 2 and can be described as follows. The target image S corresponds to study C, and the template image T corresponds to one of the other studies A, B, D, or E. For each voxel located at $\vec{x}$ in study S, the transformation $\vec{x}' = \vec{h}_{\text{TS}}(\vec{x})$ gives the coordinates $\vec{x}'$ in the study T coordinate system of the corresponding voxel of tissue. It defines the pointwise correspondence between an image T and another image S as a function of the coordinate system of image S. As illustrated by Fig. 2, insertion of the ICT applicator causes a primary deformation of the vagina and uterus that in turn causes secondary deformations of the surrounding soft-tissue structures, such as the bladder and rectum, transforming the image T into S. The transformation $\vec{x}' = \vec{h}_{\text{TS}}(\vec{x})$ is used to transform image T into the shape of image S by mapping the intensity of image T located at $\vec{x}'$ to its corresponding location $\vec{x}$ in the coordinate system of S.

The desired transformations h_{iC} for $i \in \{A,B,C,D,E\}$ are estimated by minimizing the squared error difference between the template $\vec{T}_i(\vec{x})$, (the one being deformed) and the target $\vec{T}_C(\vec{x})$, as described by the cost function

$$C(\vec{h}_{iC}) = \sum_{k=1}^{4} \alpha_k \cdot \int_{\Omega} |T_{ik}(\vec{h}_{iC}(\vec{x})) - T_{Ck}(\vec{x}))|^2 d\vec{x} \qquad (3)$$

where the weighting constants α_k define the relative importance of each image modality. The cost function must be minimized, subject to additional mathematical constraints, to ensure that $\vec{h}_{iC}$ is a mathematically meaningful mapping. Although many models are available to constrain the transformation $\vec{h}_{iC}$ consistent with this requirement, a viscous-fluid model (19) was used to constrain the set of allowable transformations used to minimize Eq. 3, due to the large distance, nonlinear deformations of the anatomy in this application.

Image preparation and overall method

The overall procedure used to process the CT data sets is outlined in Fig. 3. The first step is to manually segment the soft-tissue structures of interest in each CT data set, as

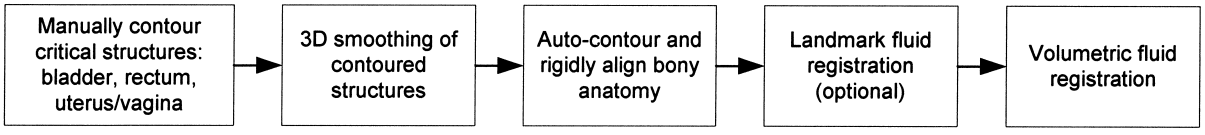

Fig. 3. Flowchart of registration method.

previously described. The contoured structures are converted to smooth 3D binary masks as described below. Then, each data set is rigidly aligned to the coordinate system of study C by rigidly aligning the pelvic bones. The rigidly-aligned data sets are then nonrigidly aligned to the coordinate system of study C, using a volumetric viscous-fluid algorithm. In some cases, the soft-tissue deformation from one study to the next is so great that the rigid registration does not provide a good initial registration for the volumetric viscous-fluid algorithm. In these cases, a semi-automatic viscous-fluid-landmark image registration (28) is performed to provide an initial nonrigid registration of the soft-tissue structures before the automatic volumetric image registration algorithm is applied.

Following manual segmentation, additional image preprocessing was performed using a commercial image processing and visualization software package, ANALYZE (AnalyzeDirect.com Inc., Lenexa, KS), as follows:

1. The image intensity was converted from 16- to 8-bit data, using an 800–1,200 intensity window.
2. The pelvic bone was segmented using a threshold of 212 and was manually edited as needed.
3. Each 3D image (A, B, D, and E) was rigidly registered to the target image C by matching the surface of the pelvic bone segmentation using the surface-match algorithm (29) implemented in ANALYZE. The intensities in the reformatted image were computed using trilinear interpolation.
4. Each stack of manually-segmented contours was converted to a binary-valued volume by filling in the contours.
5. Each template anatomic structure, represented by its binary volume, was transformed into the coordinate system of image C using the rigid registration found above, using nearest-neighbor interpolation.
6. The binary volumes were smoothed using a first-order Butterworth lowpass filter (512×512 image with cutoff frequency 24) and converted back to a binary image by thresholding, such that the original volume of the structure was maintained (30).
7. The images were cropped to a $192 \times 192 \times 64$-voxel region of interest that contained the rectum, uterus, vagina, and bladder.

Volumetric viscous-fluid registration technique

The studies A, B, D, and E were nonrigidly registered to the coordinate system of study C, using the volumetric viscous-fluid image registration technique (19). The viscous-fluid continuum mechanical model allows the shape of the template study to be nonrigidly registered to the shape of a target data set, while maintaining the topology of the deforming structures even during the large nonlinear deformations characteristic of ICT insertion. Because continuum mechanical models such as linear elasticity and thin-plate splines are linearized models containing a small deformation assumption (19), they are not well suited for this application (19). Transformations derived from the viscous-fluid model are diffeomorphic; for example, are continuous, one-to-one, onto, and differentiable. The viscous-fluid algorithm is an iterative algorithm and has the property that it does not penalize solutions involving large deformations. The viscous-fluid model is derived from Newtonian mechanics on the assumption that the restoring force is proportional to the velocity of the transformation. In contrast, the elastic deformation model assumes that the restoring force is proporportional to linear deformation, similar to a compressed or deformed spring. Thus, large displacements of a voxel from its original position are penalized (19), often preventing an image from fully being transformed into the shape of a target image.

The time-dependent viscous-fluid flow model is described by a modified Navier-Stokes equation (19):

$$\mu\nabla^2 \vec{v}_{iC}(\vec{x},t) + (\lambda + \mu)\vec{\nabla}(\vec{\nabla} \cdot \vec{v}_{iC}(\vec{x},T)) + \vec{b}(\vec{x},\vec{h}_{iC}(\vec{x},t)) = 0 \quad (4)$$

where μ and λ are viscosity constants, $\vec{v}_{iC}(\vec{x},t)$, is the velocity of deforming template $i \in \{A,B,D,E\}$ into target C at location $\vec{x}$ and time t, and $\vec{b}(\vec{x},\vec{h}_{iC}(\vec{x},t))$ is the body force at location $\vec{x}$ and time t used to deform the template. Although the body force term $\vec{b}(\vec{x},\vec{h}_{iC}(\vec{x},t))$ in Eq. 4 is a function of time, it is assumed that it is constant when solving for $\vec{v}_{iC}(\vec{x},t)$ at a fixed time t. The body force term is the Gateaux differential (31) of the multimodality cost function in Eq. 3 and is given by

$$\vec{b}(\vec{x},\vec{h}_{iC}(\vec{x},t)) = -\sum_{k=1}^{4} \alpha_k \cdot (T_i(\vec{h}_{iC}(\vec{x},t)) - T_C(\vec{x})) \cdot \vec{\nabla} T_i|_{\vec{h}_{iC}(\vec{x},t)} . \quad (5)$$

At each spatial location $\vec{x}$, $\vec{b}(\vec{x},\vec{h}_{iC}(\vec{x},t))$ applies a directed force to the template $\vec{T}_i(\vec{x})$, such that it deforms into the shape of the target study $\vec{T}_C(\vec{x})$ to minimize the cost function given in Eq. 3. In Eq. 5, when the deformed template $\vec{T}_i(\vec{h}_{iC}(\vec{x},t))$ has fully deformed into the shape of the target study $\vec{T}_C(\vec{x})$, the body force $\vec{b}(\vec{x},\vec{h}_{iC}(\vec{x},t))$ is equal to zero, i.e., $T_i(\vec{h}_{iC}(\vec{x},t)) - T_C(\vec{x}) = 0$. The velocity $\vec{v}_{iC}(\vec{x},t)$ of the deforming template described by Eq. 4 is zero for this condition because the body force is equal to zero, causing the algorithm to stop.

To simplify the presentation, we will temporarily drop the *iC* subscripts on the velocity and displacement variables. The deformation velocity $\vec{v}(\vec{x},t)$ of the template at time t is related to the time varying transformation $h(\vec{x},t) = \vec{x} + \vec{u}(\vec{x},t)$ by the total derivative of the displacement field $\vec{u}(\vec{x},t)$, given by the formula $\vec{v}(\vec{x},t) = \dfrac{d\vec{u}(\vec{x},t)}{dt} = \dfrac{\partial \vec{u}(\vec{x},t)}{\partial t} + \Sigma_{n=1}^{3} v_n(\vec{x},t) \dfrac{\partial \vec{u}(\vec{x},t)}{\partial x_n}$. Discretizing this expression in time gives the Euler update equation

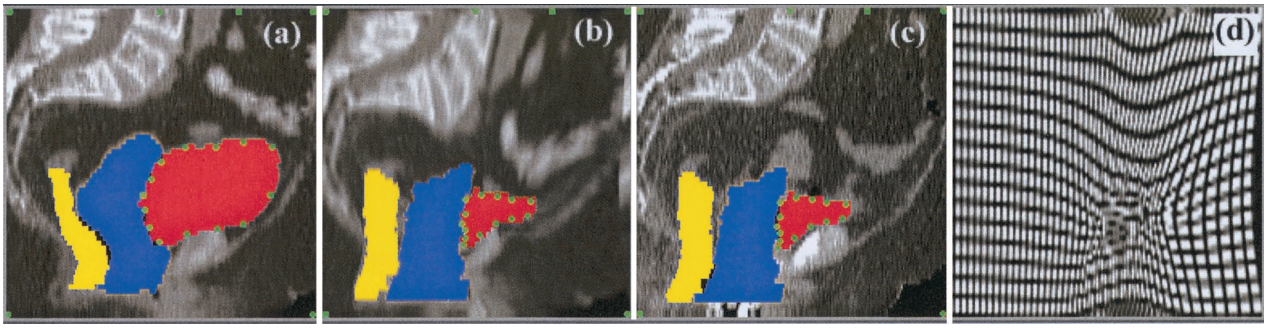

Fig. 4. The fluid-landmark registration of study A to study C for patient 2. The landmarks used for this transformation were labeled in the midsagittal plane of study A and study C, and are shown in panels (a) and (c). The resulting 2D transformation from A to C is shown in panel (b). Panel (d) shows this transformation applied to a rectangular grid.

$$\vec{u}(\vec{x},t+\delta) = \vec{u}(\vec{x},t) + \delta\vec{v}(\vec{x},t) - \delta \sum_{n=1}^{3} v_n(\vec{x},t) \frac{\partial \vec{u}(\vec{x},t)}{\partial x_n} \tag{6}$$

that is used to relate the velocity of deformation to the displacement of deformation over a δ increment of time. The subscripts in Eq. 6 correspond to the n^{th} vector component of the vectors v and x, respectively.

The volumetric fluid registration algorithm is summarized as follows. At time $t = 0$, the displacement field $\vec{u}_{iC}(\vec{x},0)$ is initialized to zero and the body force is computed using Eq. 5. Equation 4 is solved for the velocity at time $t = 0$ using Fast Fourier Transforms (32). Equation 6, representing the Euler integration step, is used to solve for the displacement field at time $t = t + \delta$. The steps of computing the body force, solving for the instantaneous velocity, and computing the Euler integration are repeated for a fixed number of time steps or until the body force term falls below a threshold. A more detailed discussion of the algorithm is given in Christensen *et al.* (19). The volumetric fluid algorithm took approximately 4.5 h to run on an SGI Origin2, using one 195-MHz R10000 processor for 400 iterations and 192 × 192 × 64-voxel image volume. The viscosity parameters used in Eq. 4 were $\mu = 1$ and $\lambda = 1$, the weights in Eq. 5 were $\alpha_k = 1$, the initial time step used in Eq. 6 was $\delta = 10^{-5}$, and the template propagation threshold was set to a Jacobian value of 0.5 (19). The viscosity parameters were selected manually. Future studies should be done to determine the effect of these parameters. In our limited experience, changing the ratio of these parameters seems to have little effect on the results.

Fluid-landmark registration technique

Often, rigid registration of the pelvic bone so poorly matches the soft-tissue structures, that it does not provide adequate initial conditions for the volumetric viscous-fluid algorithm. In these cases, a nonrigid registration is required to partially align the soft-tissue structures before the volumetric fluid registration algorithm can be applied. In this work, a fluid-landmark image registration algorithm (28, 33–35) was used instead of a standard thin-plate spline or linear-elastic landmark registration, because of the need to occasionally accommodate nonlinear deformations. The fluid-landmark image registration algorithm is similar to the volumetric fluid algorithm previously described, in that it uses the same mechanical model. However, the correspondence between images is defined by a set of corresponding landmarks instead of by a difference of intensities cost function.

The fluid-landmark algorithm requires substantially fewer parameters to describe the transformation than the volumetric viscous-fluid algorithm. The smaller number of parameters in the landmark case makes it possible to solve the Navier-Stokes equation in all four dimensions (three spatial dimensions and one time dimension) simultaneously. This approach is not practical for the full volumetric method, due its large memory and computing-time requirements, requiring us to approximate the 4D solution with a 3D spatial solution combined with Euler integration in the time dimension. The drawback of approximating the 4D solution with a 3D solution is that the final registration may contain some spatial distortion. Because these distortions grow with the extent of the deformation, we hypothesize that their effect can be diminished by using the full 4D fluid-landmark solution to provide improved initial conditions for the full volumetric Navier-Stokes algorithm.

The fluid-landmark algorithm registers a template image to a target image by matching a set of N corresponding landmarks defined in the template and target coordinate systems (see Fig. 4). Let the template landmark set be denoted as $I_0 \equiv \{\vec{y}_n\}_{n=1}^{N} \subset \Omega$ and the corresponding landmark set in the target image as $I_1 \equiv \{\vec{x}_n\}_{n=1}^{N} \subset \Omega$. . The time interval over which the fluid-landmark algorithm is minimized is assumed to be [0,1].

The landmark-matching algorithm estimates the Lagrangian transformation ϕ_{ij} from coordinate system i to coordinates system j in contrast to the Eulerian transformation $\vec{h}_{ij}$ from coordinate system i to coordinate system j. The final Lagrangian transformation $\vec{x} = \vec{\phi}_{ij}(\vec{y},1)$ and the final Eulerian transformation $\vec{y} = \vec{h}_{ij}(\vec{x},1)$ are equivalent representations because they are inverses of one another. The Lagrangian transformation is defined to be the identity

mapping $\vec{\phi}_{ij}(\vec{y},0) = \vec{y}$ at time $t = 0$ and is defined to map landmark $\vec{y}_n$ to landmark $\vec{x}_n$ at time $t = 1$, i.e., $\vec{\phi}_{ij}(\vec{y}_n,1) = \vec{x}_n$ for $n \in \{1, \ldots, N\}$.

The Lagrangian transformation is related to the Eulerian velocity field $\vec{v}_{ij}(\vec{x},t)$ by the formula

$$\vec{\phi}_{ij}(\vec{x},t) = \vec{x} + \int_0 \vec{v}_{ij}(\vec{\phi}_{ij}(\vec{x},s),s)ds. \quad (7)$$

The optimal fluid-landmark transformation from coordinate system i to j is defined as the one that minimizes the cost function

$$C(\vec{v}_{ij}(\vec{x},t)) = \int_0^1 \int_\Omega \|L\vec{v}_{ij}(\vec{x},t)\|^2 d\vec{x}dt + \sum_{n=1}^{N} \beta_n \|\vec{x}_n - \vec{\phi}_{ij}(\vec{y}_n,1)\|^2 \quad (8)$$

where $L = diag\ (-\vec{\nabla}^2 + c)$ is a diagonal 3×3 Laplacian operator differentiating in space and c is a constant. The first term of the cost function penalizes large gradients of the velocity field $\vec{v}_{ij}(\vec{x},t)$ over space and time, thereby ensuring that $\vec{\phi}_{ij}(\vec{y},t)$ is a smooth transformation, as defined by Eq. 7. The second term of the cost function forces the algorithm to match the landmarks so that $\vec{\phi}_{ij}(\vec{y}_n,1) = \vec{x}_n$ at the final instant of time. The constants β_n are weights that balance the smoothness of the velocity field with the need to enforce correspondence of each landmark in the final transformation. Normally, all of the β_n coefficients are set to the same value.

As shown by Joshi *et al*. (28, 33–35), the cost function defined in Eq. 8 only needs to be minimized for the N landmark trajectories

$$\Phi(t) = [\vec{\phi}_{ij}(\vec{y}_1,t)\vec{\phi}_{ij}(\vec{y}_2,t), \ldots, \vec{\phi}_{ij}(\vec{y}_N,t)]^\dagger \quad (9)$$

instead of $\vec{\phi}_{ij}(\vec{y},t)$ at all points $\vec{y} \in \Omega$ and time $t \in [0,1]$. The landmark trajectory $\vec{\phi}_{ij}(\vec{y}_k,t)$ describes the spatial position in Ω at time t of the landmark that originated from the point $\vec{y}_k$ at time $t = 0$. This greatly reduces the dimensionality of the problem. The fluid-landmark transformation $\vec{x} = \vec{\phi}_{ij}(\vec{y},1)$ for all $\vec{y} \in \Omega$ is computed from the landmark trajectories using the procedure outlined in Appendix A.

Selection of landmarks on 3D surfaces identifying corresponding points on the boundaries of smooth objects is a difficult task. To simplify this problem, selection of corresponding landmark points between the two 3D images was limited to the 2D midsagittal contours of the vagina, uterus, and bladder. This 2D implementation of the fluid-landmark algorithm assumes that these organs are symmetric about the midsagittal plane. The resultant 2D transformation, strictly applicable only to the midplane sagittal slice, was assumed to apply to all parasagittal slices, effectively creating a 3D transformation. While both selection of corresponding points and replicating the 2D midsagittal transformations introduce large errors, their influence is minimized because this registration is used only as an initial condition for the full 3D volumetric fluid image registration.

The fluid-landmark algorithm took less than 1 minute to compute a 192×64-pixel transformation on an SGI Origin2 using one 195-MHz R10000 processor for 13 landmarks, 8 discrete time points, and 500 iterations of gradient descent. The parameters used were 0.1 for the gradient descent step size, and $c = 6.25 \times 10^{-6}$. The 2D transformation was extended to a $192 \times 192 \times 64$-voxel 3D transformation by replicating the 2D transformation for each sagittal plane in the region of interest.

Study endpoints

Several endpoints were used to evaluate each of the 12 transformations (mapping studies A, B, D, and E to study C for patients 1–3). First, 2D sagittal and transverse slices through the 3D-image volumes of the template, the deformed template, and the target study were visually compared. More quantitatively, the coincidence, or overlap, between the registered organs from studies A, B, D, and E and the corresponding organs in study C was evaluated. This was computed using the coincidence index, CI defined as

$$CI(i,k) = \frac{\int_\Omega T_{ik}(h_{iC}(\vec{x}))T_{Ck}(\vec{x})d\vec{x}}{\int_\Omega max\{T_{ik}(h_{iC}(\vec{x})),T_{Ck}(\vec{x})\}d\vec{x}} \quad (10)$$

for all studies $i \in \{A,B,C,D,E\}$ and object masks $k \in \{2,3,4\}$. CI is zero for completely disjoint structures, and unity for structures that exactly coincide. The increased CI for viscous-fluid deformation relative to that derived from the best rigid alignment of bony anatomy quantifies the benefit of locally deformable image registration. In addition, linear displacement of each tissue voxel from its position defined by rigid bony alignment due to use of the viscous-fluid 3D algorithm was calculated. For each contoured organ, the frequency distribution of voxel displacements was calculated and plotted and the mean voxel displacement calculated. These endpoints estimate the influence of local deformation in this application, or equivalently, the geometric error due to approximating organ shift by the conventional global transformation method.

RESULTS

Figures 5 and 6 show the registration results for the 3D CT volumes at the midsagittal slice for the first two patients. The left column shows the template studies A, B, D, and E, in rows 1, 2, 3, and 4, respectively, while the third column shows the target study C (each panel in column three are

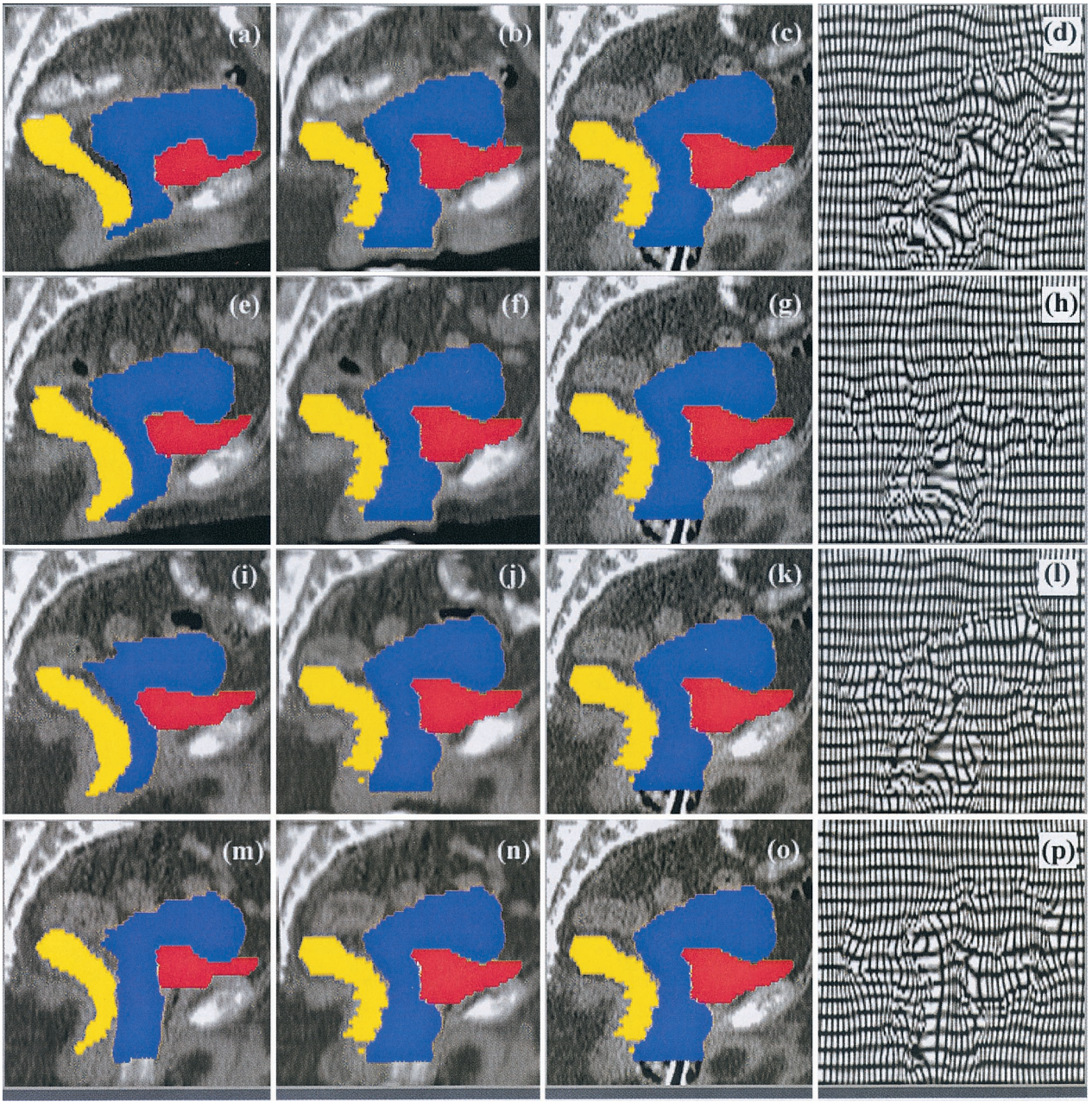

Fig. 5. Results from the four, 3D viscous-fluid image registrations computed for patient 1. Row 1 shows the midsagittal CT slices from the registration of study A to study C: (a) study A, (b) study A transformed to shape of study C, (c) study C, (d) A-to-C transformation applied to a rectangular grid. The rectum (yellow), vagina/uterus (blue), and bladder (red) binary masks used to generate the transformations are shown superimposed on the CT data. The deformed grid was computed using the displacement fields tangent to the midsagittal plane, ignoring the displacement normal to the midsagittal plane. Rows 2, 3, and 4 show the same information as row 1 for the registration of B-to-C, D-to-C, and E-to-C, respectively.

identical). The second column shows the midsagittal slice (A, B, D, and E in rows 1–4) deformed by the appropriate 3D transformation $\vec{h}_{iC}$ so as to be in voxel-to-voxel registration with study C. Notice that the transformed binary masks shown in the second column look nearly identical to those in the third column, indicating a good registration of the data sets. The fourth column shows the transformation applied to a rectangular grid at the level of the midsagittal slice. These grids visualize how each template data set was transformed into the shape of the target data set at the level of the midsagittal plane. These grids approximate the effect of the 3D transformation at this slice, because most of the soft-tissue deformation is symmetric about the midsagittal plane. The grids show that the anatomy was smoothly deformed into the shape of the target data set study C. The grids also show that the transformations are continuous and one-to-one, because the grid lines do not cross one another.

Due to the large shape difference between the bladder

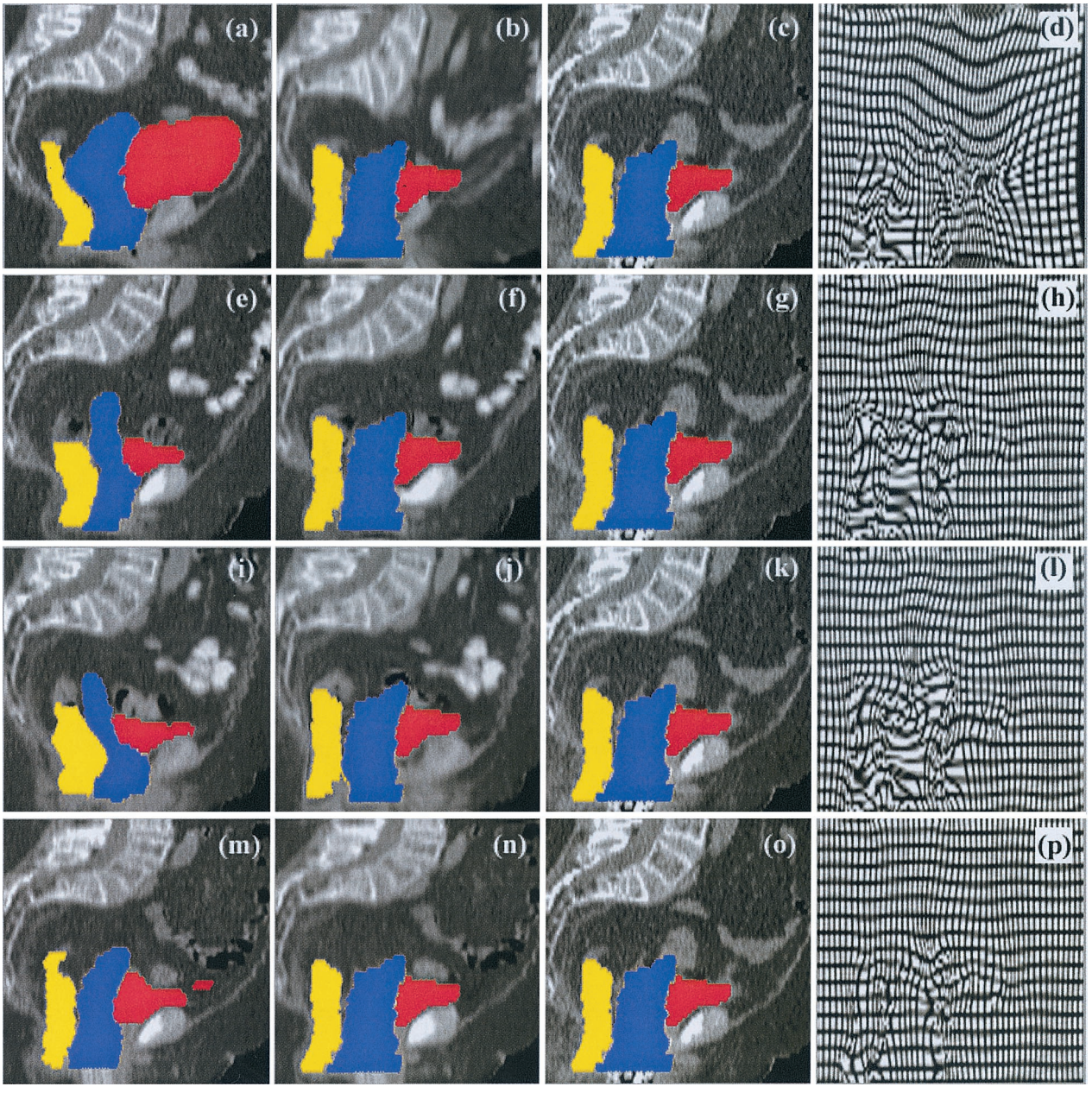

Fig. 6. Results from the four, 3D viscous-fluid image registrations computed for patient 2. See the caption of Fig. 5 for the description of the panels.

volume contents in study A and C for patient 2, the viscous-fluid-landmark registration was used to provide an initial nonrigid registration before applying the volumetric viscous-fluid algorithm. Figure 3 shows the midsagittal slice from study A and C, along with the 14 landmark points (see green dots) used to define the viscous-fluid-landmark transform. The second panel of Fig. 3 illustrates application of the 2D fluid-landmark transformation to the sagittal cross-section of study A, while the fourth panel shows its effect on a rectangular grid. This 2D transformation was applied to each sagittal slice of study A, producing a 3D transformation. The landmark-transformed study A image was then further deformed to match target study C by the volumetric fluid algorithm. The transformations produced by the viscous-fluid-landmark and volumetric algorithms were concatenated together to produce the final nonrigid transformation used to transform study A to C, as shown in panels (b) and (d) of Fig. 5.

Figures 7, 8, and 9 show the midsagittal registration results of studies A, B, and E to study C, respectively, for patient 3. To successfully register patient 3's soft-tissue structures required two transformations, due to the large deflection of the vagina and uterus in study C. One transformation, consisting of 2D landmark transformation followed by the 3D viscous-fluid transformation using only the bladder binary mask, was used to track the deformation of the bladder (top row of each figure) and independently using the same procedure to track the deformation of the vagina,

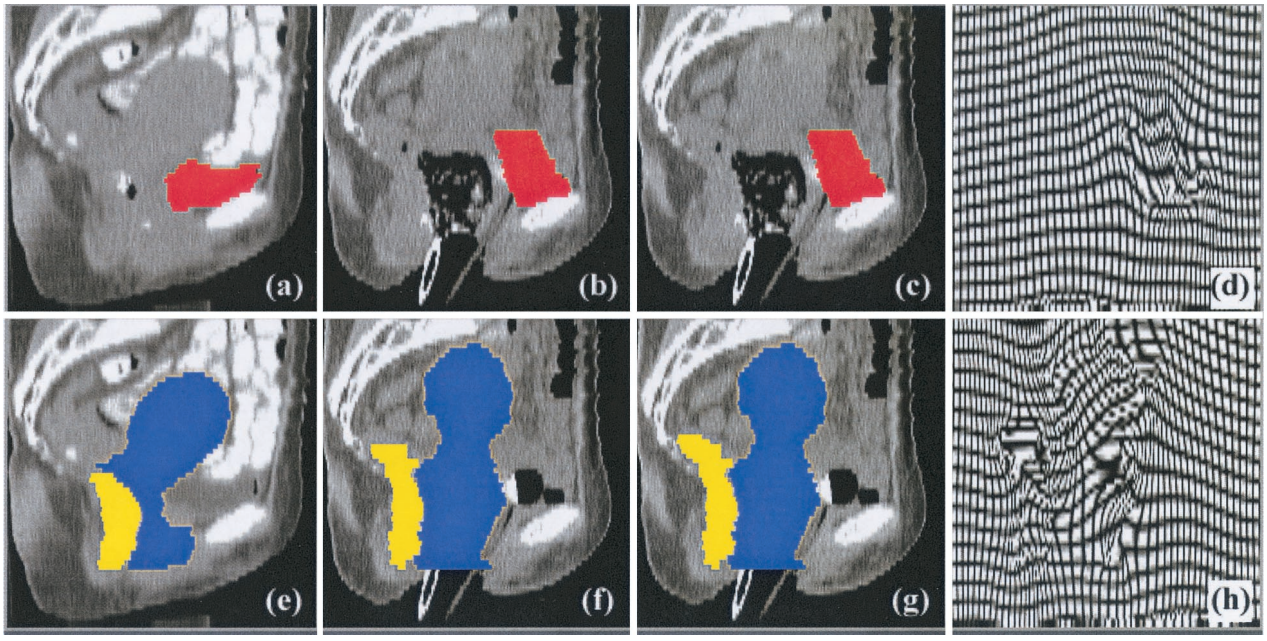

Fig. 7. A-to-C transformations for patient 3. Row 1 shows the midsagittal slices from the 3D A-to-C registration generated by matching bladder binary mask (red) only. Row 2 shows the midsagittal slices from the 3D A-to-C registration generated from matching the rectum (yellow) and vagina/cervix (blue) binary masks. These results were generated using the fluid-landmark initialization followed by volumetric fluid registration. The fluid-landmark algorithm used 5 landmarks identified along the midsagittal contour of the bladder and 10 landmarks identified along the midsagittal contour of the vagina/uterus. (a) Study A CT and bladder mask, (b) bladder mask A transformed with A-to-C transformation superimposed on CT from study C, (c) study C CT and bladder mask, (d) A-to-C transformation applied to a rectangular grid. Panels (e–h) are defined similarly.

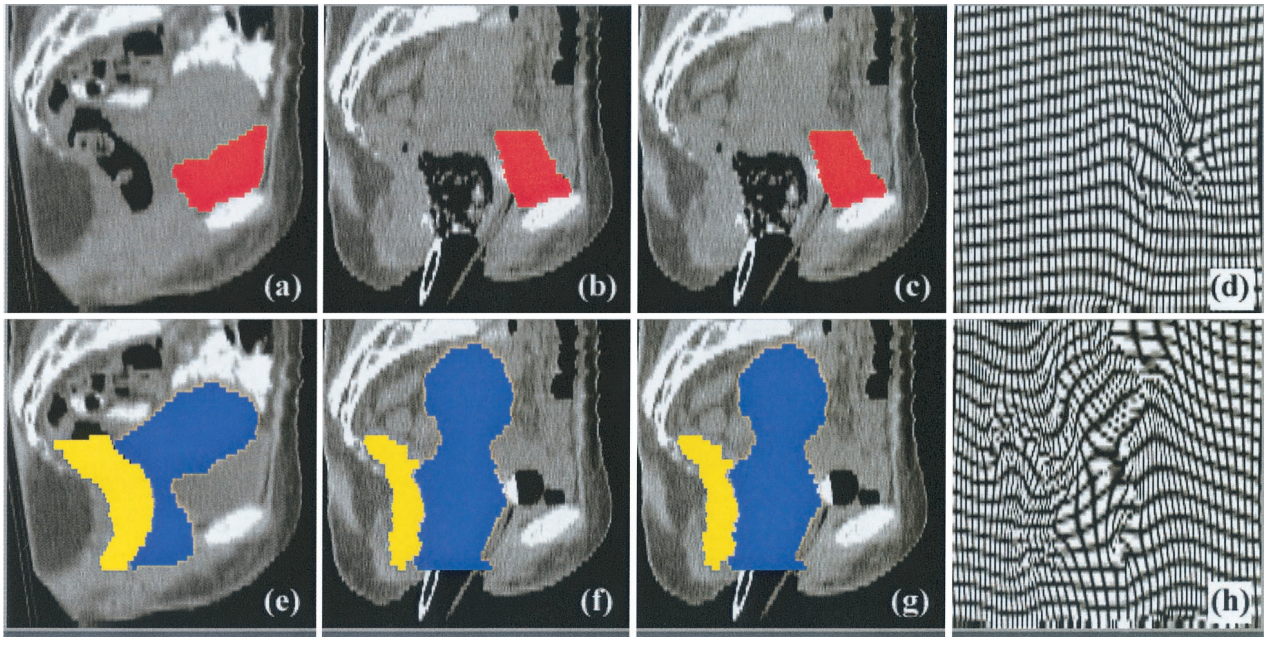

Fig. 8. B-to-C transformations for patient 3. See caption of Fig. 7 for a description of the panels. The fluid-landmark algorithm used 6 landmarks identified along the midsagittal contour of the bladder and 13 landmarks identified along the midsagittal contour of the vagina/uterus.

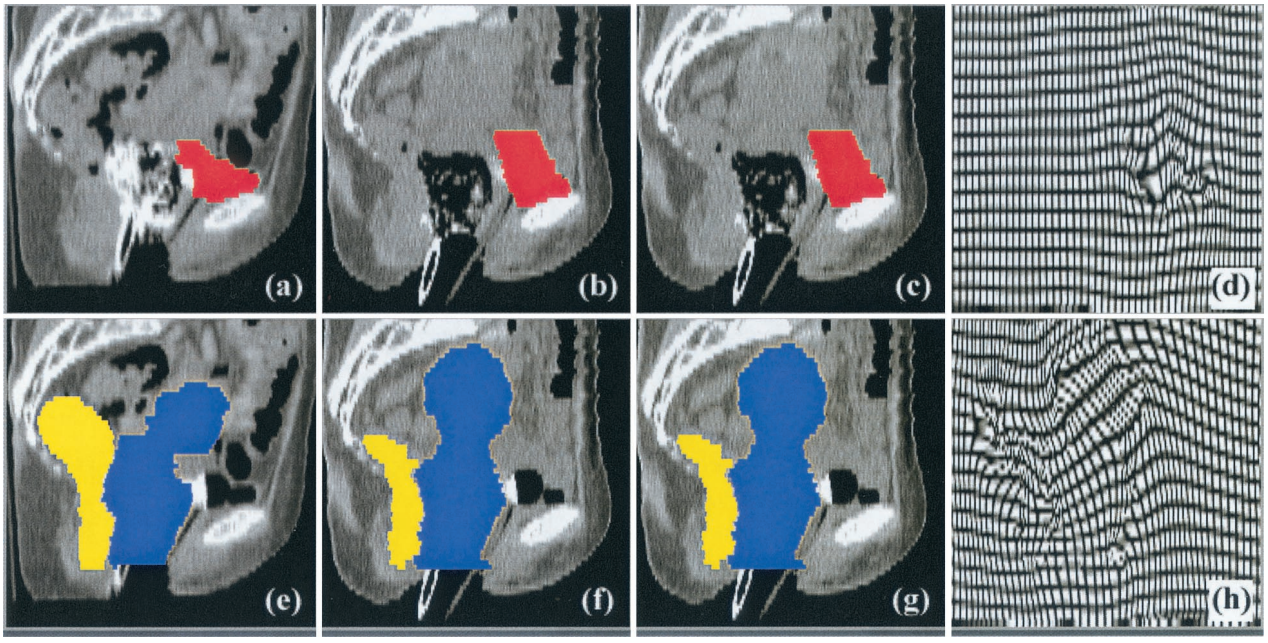

Fig. 9. E-to-C transformations for patient 3. See caption of Fig. 7 for a description of the panels.

uterus, and rectum. This resulted in different transformations for the two sets of organs because the independent landmark transformations defined different initial conditions for the 3D viscous-fluid transform. This is required because the continuous nature of the viscous-fluid model is not well suited to modeling deformations involving separation of organs (e.g., uterus and bladder) sharing a common border in the template image but not in the target image (see Fig. 7). The gray-scale CT image intensity data outside the contoured structures were not used to compute any of the transformations for patient 3.

In all cases, the transformed binary masks shown in the second column of Figs. 4 through 9 look nearly identical to the binary masks in the third column. This observation can be made quantitative for the 3D segmentations using the coincidence index (See Table 1). The low coincidence indices associated with the rigid registration demonstrate that alignment of the data sets using only the pelvic bones does not give a satisfactory registration of the data sets. On the other hand, the coincidence indices that are nearly equal to one for the fluid registrations demonstrate that the viscous-fluid model is able to accommodate the nonrigid soft-tissue deformation associated with ICT brachytherapy.

Table 2 provides the mean linear voxel displacement relative to the pelvic bone rigid image registration. This table demonstrates that the average motion of a particle of the bladder, rectum, and uterus/vagina moved from 2.8 to 28.1 mm for the three patients used in this study. As expected, the uterus/vagina moves the most, on average.

Figures 10, 11, and 12 show normalized histograms of voxel displacement relative to their positions defined by rigid bony alignment for the bladder, rectum, uterus/vagina, and the uncontoured anatomy for the experiments. In all cases, the histogram demonstrates that voxel

Table 1. Coincidence index after rigid and fluid alignment

		Bladder		Rectum		Uterus/Vagina	
Patient	Registration	Rigid alignment	Fluid alignment	Rigid alignment	Fluid alignment	Rigid alignment	Fluid alignment
1	A to C	0.581	0.991	0.416	0.989	0.498	0.997
	B to C	0.722	0.998	0.443	0.980	0.702	0.999
	D to C	0.646	0.990	0.379	0.983	0.590	0.996
	E to C	0.507	0.997	0.533	0.999	0.642	0.997
2	A to C	0.160	0.998	0.216	0.990	0.338	0.991
	B to C	0.525	0.997	0.102	0.988	0.352	0.971
	D to C	0.426	0.996	0.109	0.951	0.263	0.906
	E to C	0.460	0.997	0.482	0.999	0.576	0.998
3	A to C	0.420	0.997	0.052	0.813	0.366	0.998
	B to C	0.428	0.997	0.121	0.991	0.246	0.997
	D to C	N/A	N/A	N/A	N/A	N/A	N/A
	E to C	0.661	1.000	0.276	0.992	0.510	0.998

Table 2. Mean linear voxel displacement relative to the best rigid alignment

Patient	Registration	Mean voxel displacement (mm)			
		Uncontoured anatomy	Bladder	Rectum	Uterus/ Vagina
1	A to C	1.6	5.1	5.0	6.1
	B to C	0.5	2.8	4.4	2.9
	D to C	0.9	3.9	5.0	4.0
	E to C	0.8	5.4	4.1	3.6
2	A to C	12.7	28.1	8.0	13.1
	B to C	0.8	3.5	10.5	6.7
	D to C	0.8	5.1	9.3	7.7
	E to C	0.5	3.5	3.1	3.8
3	A to C	N/A	15.4	15.6	19.1
	B to C	N/A	9.1	16.2	24.1
	D to C	N/A	N/A	N/A	N/A
	E to C	N/A	5.4	13.2	15.0

displacement is highly variable, with the most probable displacement centered about the average displacement. Voxels are relatively stationary near the vaginal introitus and anus and move more freely near the uterine fundus. These histograms show that the distributions of displacements in the bladder, rectum, and uterus/vagina are broad and are not well characterized by a single rigid registration. These histograms also suggest that there is relatively little motion of the uncontoured anatomy. One reason for this is that the CT images do not contain sufficient information about the uncontoured soft-tissue structures, such as the small bowel, to adequately assess coincidence. The apparent large displacement of the uncontoured anatomy in studies A–C in patient 2 is due to the fluid-landmark initialization. In this case, the sur-

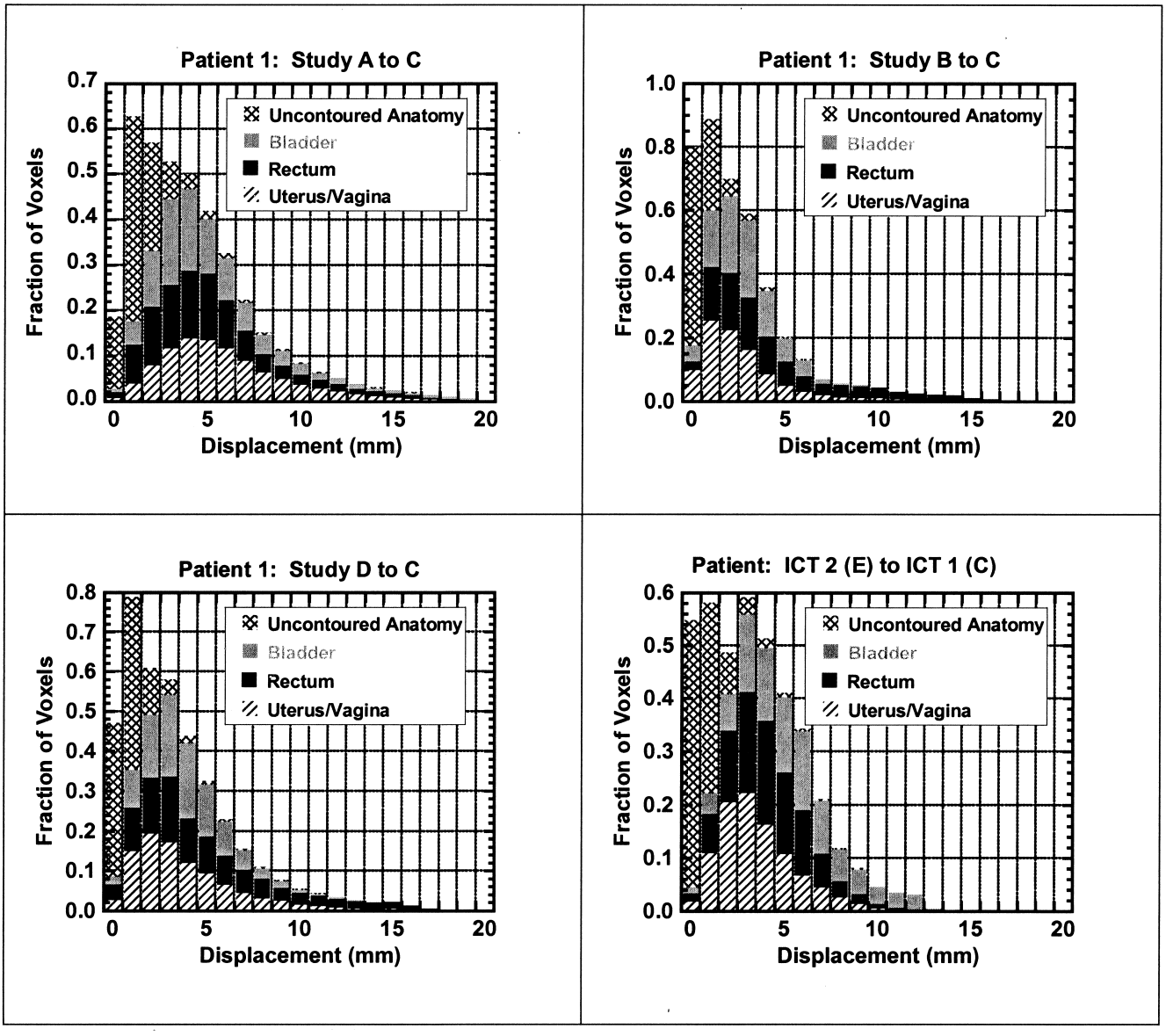

Fig. 10. Histograms of voxel displacement, produced by the viscous-fluid transform, relative to the rigid bony alignment for patient 1 experiments.

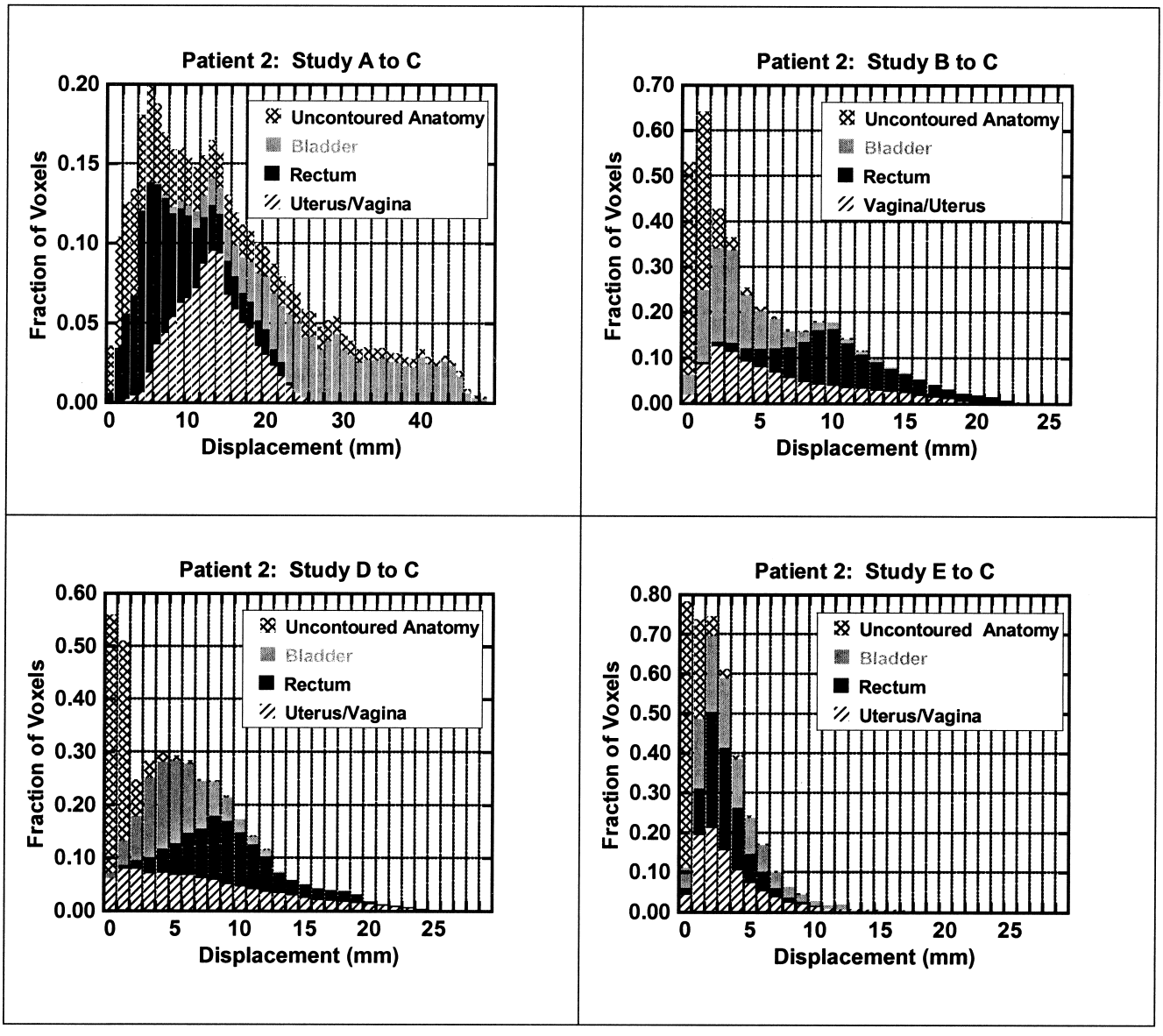

Fig. 11. Histograms of voxel displacement, produced by the viscous-fluid transform, relative to the rigid bony alignment for patient 2 experiments.

rounding structures were deformed by the fluid-landmark registration to match the structures of interest.

The need to provide the volumetric viscous-fluid algorithm with good initial conditions is illustrated in Fig. 13. This figure shows the result of transforming study C to study B for patient 3, as viewed at the midsagittal plane, as a function of time. The black arrows show that the study C uterine fundus (here taken to be the template) collapses into the endocervix of target study B, while the anterior wall of the template uterus stretches to match the study B fundus (white arrow). This result clearly demonstrates that an apparently "good" match between initial and final template binary masks can be achieved with an anatomically nonsensical deformation process. Use of the 2D fluid-landmark algorithm successfully imposes physician-specified inexact constraints on the subsequent 3D deformation process. Such nonsensical deformation models can be easily identified by examining the deformed 3D grids. These grids indicate that patients 1 and 2 (excluding patient 2's bladder) do not need more refined initial conditions to be specified.

DISCUSSION

We have applied a novel image-registration technology, the viscous-fluid transformation method, to the challenging problem of registering serial-imaging studies characterizing a patient's anatomy during a 6–7-week course of definitive radiotherapy for locally advanced cervix cancer. Because our method simulates soft-tissue deformation as a viscous-fluid flow problem, it can accommodate large-scale tissue

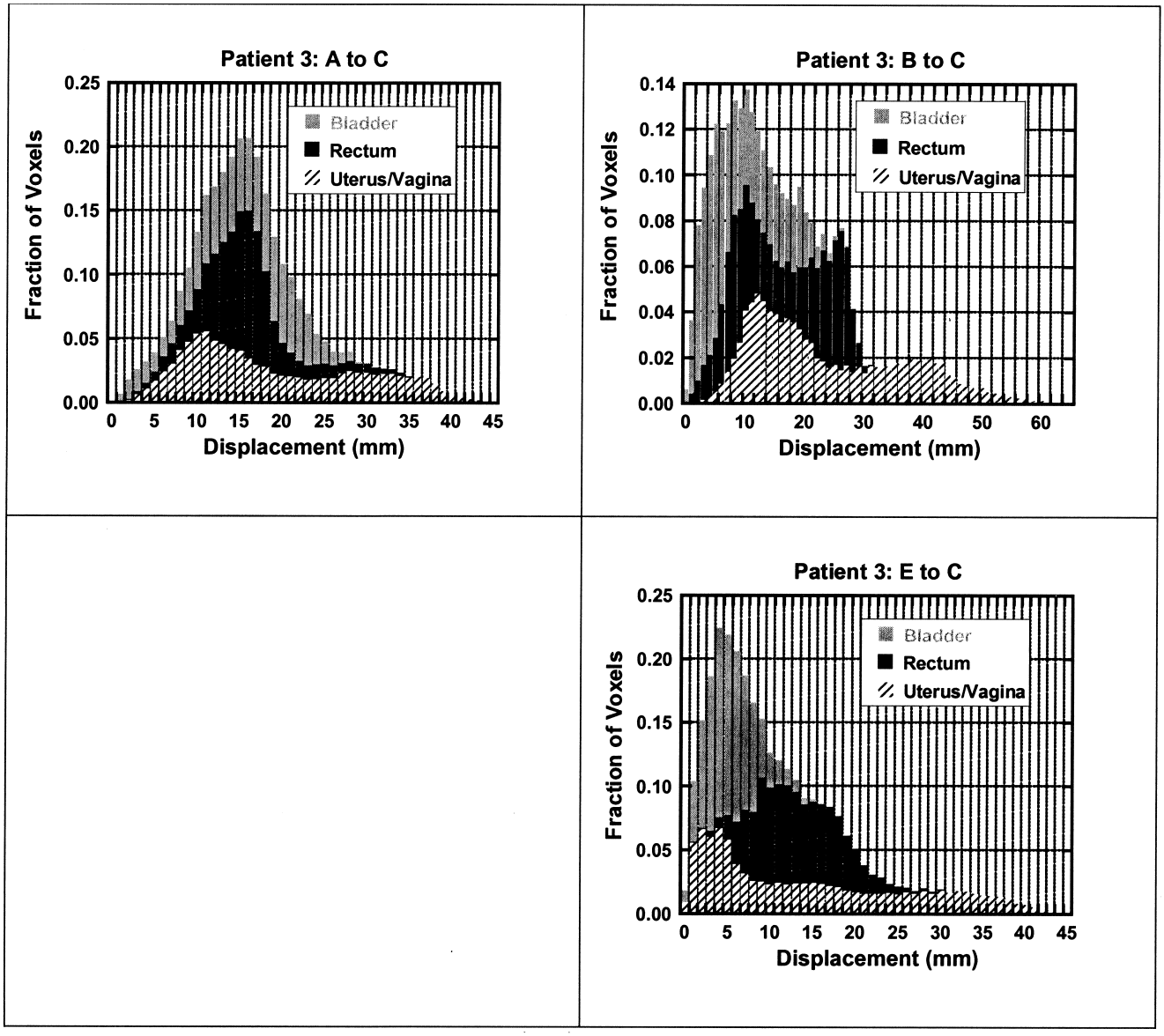

Fig. 12. Histograms of voxel displacement, produced by the viscous-fluid transform, relative to the rigid bony alignment for patient 3 experiments. Study D was missing for patient 3; therefore, there is no histogram for D to C.

deformations. It is therefore a significant improvement over the rigid affine transformation model and the linear elastic deformable anatomy approach. To our knowledge, our work is the first effort to apply the viscous-fluid transformation approach to soft-tissue structures outside the brain. The pelvis is a much more challenging application because of (a) lower soft-tissue contrast and more indistinct anatomic borders, (b) significantly more variation of signal intensity within anatomic structures and from study-to-study, and (c) much larger variations in organ shape and relative location. We have produced plausible voxel-to-voxel registrations in the face of even massive distortion and rearrangement of soft-tissue following intracavitary applicator insertion and removal.

Our work is the first to use deformable anatomy image-registration techniques to transform serial pelvic CT studies obtained with and without intracavitary applicator systems in place into a single anatomically consistent frame of reference. This allows the deformed dose distributions to be summed in registration with the underlying anatomy. In so doing, we have quantitatively estimated the magnitude of localized tissue deformation and displacement associated with intracavitary brachytherapy. Relative to the best rigid alignment of serial-imaging studies, individual tissue voxel displacement averages 3 to 20 mm and can be as large as 60 mm. Given the large dose gradients (8–15%/mm) characteristic of intracavitary brachytherapy, cumulative organ doses evaluated using conventional affine image registration would likely be highly inaccurate. Thus, development and validation of deformable image registration techniques are essential to the integration of 3D imaging into the planning and

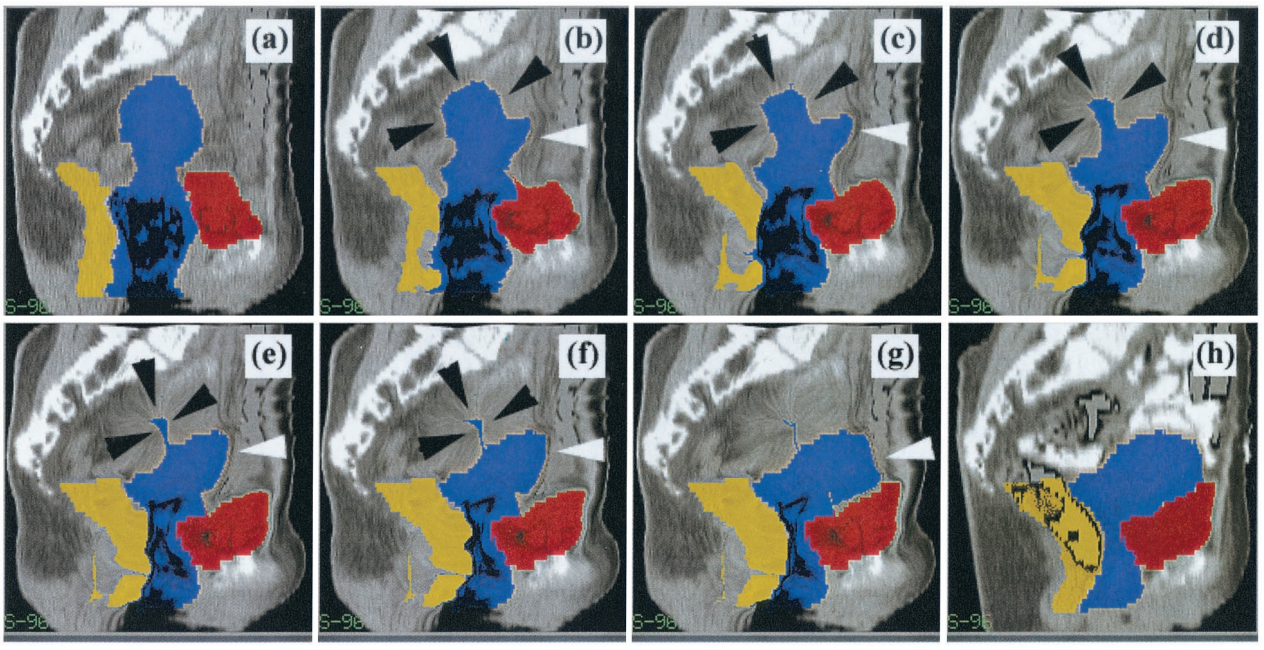

Fig. 13. Example of a failed 3D fluid transformation from patient 3 study C to study B when fluid-landmark initialization was not used. The panels show the midsagittal slice from the fluidly deforming template at (a) 0, (b) 50, (c) 100, (d) 200, (e) 300, (f) 400, and (g) 1,000 iterations. The midsagittal slice from the target data set is shown in panel (h). The black arrowheads show where the uterus was incorrectly compressed, and the white arrowheads show where the uterus was incorrectly expanded to match the target data set.

evaluation of any course of therapy combining multiple intracavitary insertions with external-beam radiotherapy. These problems are especially severe for our treatment technique (3, 26), which relies heavily on highly nonuniform external beam dose distributions produced by multiple-layer midline blocks. An important extension of this work will be to use the viscous-fluid transformations to compute the cumulative dose distributions for each patient in the reference frame of study C. A dose distribution associated with each CT study will be mapped to the coordinate system of study C and summed, yielding the estimated cumulative dose distribution in one-to-one correspondence with the underlying anatomy. Assuming that this distribution is the most accurate representation available of the dose distribution actually delivered to the patient, the accuracy of the expected dose distribution, calculated without the benefit of 3D imaging, or that derived from rigidly registered CT images, can be retrospectively evaluated. It is hoped that use of this method will yield better-defined dose-volume-response relationships and will provide the basis for improving patient outcome through physical optimization of the dose distribution.

Although the viscous-fluid transformation model tracks pelvic soft-tissue deformation in a plausible fashion, it is in an early stage of development and has several limitations. Specifically, the viscous-fluid model deforms the anatomy from one CT volume to another based purely on its mathematical properties, and does not attempt to accurately model the true biomechanical properties of the pelvic structures. As such, there was no attempt made to pick parameters that have any physical meaning. In addition, the entire pelvic anatomy was modeled using the same parameters, with no distinction between different types of structures or biologic tissue. Thus, there is no guarantee that and $\vec{x}$ *and* $\vec{h}_{iC}(\vec{x})$ describe the same voxel of biologic tissue when $i \neq C$. To improve the physical accuracy of our transformations, we plan to include additional *a priori* information into the registration model to give more physically accurate registrations. Both outer and inner boundaries of structures will be included in the model, allowing different continuum mechanical models to deform the inner and outer surfaces of structures. This will allow mass gains and losses to be constrained to the interiors of the bladder, rectum, and vagina. Boundary conditions will be included to allow adjacent structures to separate from one another and to allow structures to slip and slide against one another's surfaces. This should overcome the limitation of needing multiple transformations, such as in the case of patient 3, when the uterus and bladder separated from one another from one time instance to another. Finally, the current procedure requires manual placement of landmarks. Not only is this a time-consuming step, but it also introduces another source of error. In the future, we plan to investigate automatic methods for generating initial conditions, such as using a linear elastic registration model (23). Finally, physical verification of matching accuracy, as evaluated in deformable phantoms and animal subjects, is an important future activity.

CONCLUSION

Patient soft-tissue structures undergo large deformations and displacements during the external beam, multiple ICT course of radiotherapy typically prescribed for locally advanced cervix cancer. These changes cannot be modeled by the conventional rigid-landmark transformation method. We have described a novel method, the viscous-fluid transformation method, which accommodates local deformation and displacement of soft-tissue structures, based upon continuum-mechanics models of the deformation process. This method produces anatomically plausible 3D registrations between imaging studies with and without intracavitary applicators in place, or between studies documenting different insertions in the same patient. Despite the limitations of its current implementation, the viscous-fluid transformation method is a promising solution to what heretofore has been regarded as an almost intractable image registration problem. The viscous-fluid transformation method may allow rigorous integration of CT and MR imaging into the planning and evaluation combined intracavitary brachytherapy and external-beam therapy, of gynecological malignancies.

APPENDIX A

Summary of the fluid-landmark registration algorithm

The complete description of the fluid-landmark image-registration algorithm can be found in Joshi and Miller (28) and is summarized here.

The fluid-landmark transformation $\vec{x} = \vec{\phi}_{ij}(\vec{y},1)$ for $\vec{x},\vec{y} \in \Omega$ that transforms the coordinate system of $T_i(\vec{y})$ into that of $T_j(\vec{x})$ is estimated using the flowing procedure. The boundary conditions of $\vec{\phi}_{ij}(\vec{y},t)$ enforce the landmark trajectories, to have the boundary conditions $\Phi(0) = [\vec{y}_1, \vec{y}_2, \ldots, \vec{y}_N]^{\dagger}$. Equation 8, restated in terms of the N landmark trajectories Φ, is given by

$$C(\Phi) = \int_0^1 \dot{\Phi}^{\dagger}(t)\, K^{-1}(\Phi(t))\dot{\Phi}(t)dt + \sum_{n=1}^{N} \beta_n \|\vec{x}_n - \vec{\phi}_{ij}(\vec{y}_n,1)\|^2 \quad (11)$$

where $\dot{\Phi}(t)$ is the time derivative of $\Phi(t)$ and $K^{-1}(\Phi[t])$ is a $3N \times 3N$ matrix that defines the spatial correlation between the N landmark trajectories as a function of time. The form of $K(\Phi[t])$ depends on the differential operator L used in Eq. 8. In the present case, $L = diag(-\vec{\nabla}^2 + C)$ implies that the nm^{th} 3×3 sub-block of $K(\Phi[t])$ has the form $(K(\Phi(t)))_{nm} = k(\vec{\phi}_{ij}(\vec{y}_n,t),\vec{\phi}_{kj}(\vec{y}_m,t))$, where $k(\vec{x},\vec{y}) = \frac{2}{\sqrt{c(2\pi)}} e^{-\sqrt{c}\|\vec{x}-\vec{y}\|^2}$ and I is the 3×3 identity matrix. The function $k(\vec{x},\vec{y}) = \frac{2}{\sqrt{c(2\pi)}} e^{-\sqrt{c}\|\vec{x}-\vec{y}\|^2}$ provides larger correlation between landmark trajectories that are close together in space at a fixed time t than trajectories that are farther apart in space. Once the landmark trajectories $\hat{\Phi}(t)$ that minimize Eq. 11 are determined, they are used to determine the Lagrangian transformation $\vec{\phi}_{ij}(\vec{y},1)$ for all $\vec{y} \in \Omega$ using Eq. 7 and

$$\vec{v}_{ij}(\vec{x},t) = \sum_{n=1}^{N} K(\vec{\phi}_{ij}(\vec{y}_n,t),\vec{x}) \sum_{m=1}^{N} (K^{-1}(\Phi(t)))_{nm} \vec{\phi}_{ij}(\vec{y}_m,t) \quad (12)$$

REFERENCES

1. DiSaia PJ, Creasman WT. Clinical gynecological oncology. 3rd ed. New York: C.V. Mosby; 1989.
2. Fletcher GH, Hamberger AD. Squamous cell carcinoma of the uterine cervix: Treatment technique according to size of the cervical lesion and extension. In: Fletcher GH, editor. Textbook of radiotherapy. 3rd ed. Philadelphia: Lea & Febiger; 1980. p. 732–772.
3. Perez CA, Fox S, Grigsby PW, *et al*. Impact of dose in outcome of radiation alone in carcinoma of uterine cervix. Analysis of two different methods. *Int J Radiat Oncol Biol Phys* 1991;21:885–898.
4. Paunier JP, Delclos L, Fletcher GH. Causes, time of death, and sites of failure in squamous cell carcinoma of the uterine cervix in intact uterus.*Radiology* 1967;88:555–562.
5. Perez CA, Kuske RR, Camel HM, *et al*. Analysis of pelvic tumor control, and impact on survival in carcinoma of the uterine cervix treated with radiation therapy alone. *Int J Radiat Oncol Biol Phys* 1988;14:613–621.
6. Kovalic JJ, Perez CA, Grigsby PW, *et al*. The effect of volume of disease in patients with carcinoma of the uterine cervix. *Int J Radiat Oncol Biol Phys* 1991;21:905–910.
7. Mitchell M, Lu J, Grigsby PW, *et al*. Pelvic radiation with concurrent chemotherapy compared with pelvic, and para-aortic radiation for high-risk cervical cancer. *N Engl J Med* 1999;340:1137–1143.
8. Chism SE, Keys HM, Gillin MT, Carcinoma of the cervix. A time dose analysis of control and complications. *Am J Roentgenol* 1975;123:84–90.
9. Perez CA, Fox S, Lockett MA, *et al*. Impact of dose in outcome of irradiation alone in carcinoma of the uterine cervix: Analysis of two different methods. *Int J Radiat Oncol Biol Phys* 1991;21:885–898.
10. Pourquier H, Deubois JB, Delard R. Cancer of the uterine cervix. Dosimetric guidelines for prevention of late rectal and rectosigmoid complications as a result of radiotherapeutic treatment. *Int J Radiat Oncol Biol Phys* 1982;8:1887–1895.
11. ICRU. Report no. 38. Dose and volume specification for reporting intracavitary therapy in gynecology. Washington, D.C.: International Commission of Radiation Units and Measurements; 1985.
12. Schoeppel SL, LaVigne ML, Martel MK, *et al*. Three-dimensional treatment planning of intracavitary gynecologic implants. Analysis of ten cases and implications for dose specification. *Int J Radiat Oncol Biol Phys* 1993;28:277–283.

13. Ling CC, Schell MC, Working KR, *et al*. CT assisted assessment of bladder, and rectum dose in gynecological implants. *Int J Radiat Oncol Biol Phys* 1987;13:1577–1582.
14. Hunter RD, Wong F, Moore C, *et al*. Bladder base dosage in patients undergoing intracavitary therapy. *Radiother Oncol* 1986;7:189–197.
15. Gebara WJ, Weeks KJ, Hahn CA, *et al*. Computed axial tomography tandem, and ovoids (catto) dosimetry. Three-dimensional assessment of bladder and rectal doses. *Radiat Oncol Invest* 1998;6:268–275.
16. Grigsby PW, Georgiou A, Williamson JF, *et al*. Anatomic variation of gynecologic brachytherapy prescription points. *Int J Radiat Oncol Biol Phys* 1993;27:725–729.
17. Eisbruch A, Williamson JF, Dickson R, *et al*. Estimation of tissue volume irradiated by intracavitary implants. *Int J Radiat Oncol Biol Phys* 1993;25:733–744.
18. Pilepich MV, Pasard S, Madoc-Jones H, *et al*. Effect of bladder distension on dosimetry in gynecological implants. *Radiology* 1981;140:516–518.
19. Christensen GE, Rabbitt RD, Miller MI. Deformable templates using large deformation kinematics. *IEEE Trans Image Processing* 1996;5:1435–1447.
20. Christensen GE, Rabbitt RD, Miller MI. 3D brain mapping using a deformable neuroanatomy. *Phys Med Biol* 1994;39: 609–618.
21. Sailer SL, Rosenman JG, Soltys M, *et al*. Improving treatment planning accuracy through multimodality imaging. *Int J Radiat Oncol Biol Phys* 1996;35:117–124.
22. Kessler ML. Integration of multimodality image data for three-dimensional treatment planning. Categorical course in three-dimensional treatment planning. 80th Annual Meeting of the Radiological Society of North America. Chicago: RSNA Publications; 1994.
23. Christensen GE, Joshi SC, Miller MI. Volume geometric transformation or mapping anatomy. *IEEE Trans Med Imaging* 1997;16:864–877.
24. Bookstein FL. The measurement of biological shape, and shape change. Lecture notes in biomathematics. vol. 24. New York: Springer-Verlag; 1978.
25. Bajcsy R, Lieberson R, Reivich R. A computerized system for the elastic matching of deformed radiographic images to idealized atlas images. *J Comput Asst Tomogr* 1983;7:618–625.
26. Williamson JF. Physics of brachytherapy. In: Perez CA, Brady LW, editors. Principles and practice of radiation oncology. 3rd ed. Philadelphia: J.B. Lippincott Co.; 1998. p. 405–468.
27. Weeks KJ, Montana GS. Three-dimensional applicator system for carcinoma of the uterine cervix. *Int J Radiat Oncol Biol Phys* 1997;37:455–463.
28. Joshi SC, Miller MI. Landmark matching via large deformation diffeomorphisms. *IEEE Trans Image Processing* 2000;9: 357–1370.
29. Pelizzari CA, Chen GTY, Spelbring DR, *et al*. Accurate three-dimensional registration of CT, PET, and/or MR images of the brain. *J Comput Asst Tomogr* 1989;13:20–26.
30. Pratt WK. Digital image processing. 2nd ed. New York: John Wiley & Sons, Inc.; 1991.
31. Luenberger DG. Optimization by vector space methods. New York: John Wiley & Sons; 1969.
32. Yin P. Image registration for brachytherapy treatment planning in radiotherapy of cervical cancer [Masters thesis]. Iowa City: The University of Iowa; 1999.
33. Joshi SC. Large deformation diffeomorphisms, and Gaussian random fields for statistical characterization of brain submanifolds [Ph.D. thesis]. St. Louis, MO: Washington University, Sever Institute of Technology; 1997.
34. Miller MI, Joshi SC, Christensen GE. Large deformation fluid diffeomorphisms for landmark, and image matching. In: Toga A, editor. Brain warping. San Diego: Academic Press; 1999. p. 115–132.
35. Grenander U, Miller MI. Computational anatomy. An emerging discipline. *Q Appl Math* 1998;LVI:617–694.